Composite Structures 160 (2017) 1126–1135

Contents lists available at ScienceDirect

Composite Structures

journal homepage: www.elsevier.com/locate/compstruct

Cohesive interface behaviour and local shear strains in axially loaded composite annular tubes

Agostina Orefice, Geminiano Mancusi *, Luciano Feo, Fernando Fraternali

Department of Civil Engineering, University of Salerno, Italy

ARTICLE INFO

Article history:
Received 26 October 2016
Accepted 27 October 2016
Available online 29 October 2016

Keywords:
Tubes
FRP
Adhesive joints
FEM

ABSTRACT

The local behaviour of a composite profile with annular cross-section is studied in presence of interfacial cohesive forces at the ends, where the lateral surface may be involved in a bonding connection. Features include the possibility of warping displacements, nonlinear shear strains within the thickness of the annular wall originated by the bonding interactions. Numerical simulations are carried out in order to investigate the tube behaviour over the loading path up to the failure, thus underlining the relevance of the thickness on the magnitude of the shear strains.

© 2016 Elsevier Ltd. All rights reserved.

1. Introduction

Thick-walled tubular composite profiles with annular cross-section represent the optimal solution for a number of applications (large truss covers, large bridge decks or spatial frames). Within this context, the possibility of connecting the composite tubes by means of co-axial nodal devices has been recently investigated with the aim of developing a standard, reliable, easy to make system for onsite assembling modality by using a structural glue.

Many factors affect the bonding behaviour at the ends of the tube, where the adhesive interface to the nodal device exists: the constitutive properties for the device (metal, composite) and the tube (GFRP, CFRP), the choice of the glue, the length and thickness of the bonding layer, the considered loading path.

A useful approach for modelling the mechanical response of the adhesive interface refers to the cohesive fracture mechanics. In this view, the interfacial interactions come from appropriate potentials thus allowing a simple mathematical formulation of the bonding problem.

The cohesive fracture mechanics literature includes many contributions over the recent years especially devoted to the bonding of composite adherents.

Almitani and Othman [1] investigated the harmonic response of single lap and double-lap joints including viscoelastic properties of the adhesive and the adherents. To this aim they assumed a viscous-elastic behaviour for the adhesive and the adherents, which is represented by a complex modulus written using the model of Kelvin-Voigt.

Xu and Qu [2] developed a model that incorporates the unloading behaviour varying from full plasticity to damage. They captured the irreversible deformation mechanisms resulting from the localized plastic deformation and damage accumulation due to the nonlinear separation of fibre–matrix interface under transverse loading and unloading conditions.

The last models are the most recent ones. However, for the specific scope of the present study, which is focused on the analysis of the local behaviour of the tube in presence of cohesive forces, we have chosen to start a discussion from two well-known papers by Rose et al. [3,4]. These works exhibit a great interest due to their universal binding energy law for studying the mode I crack propagation in metallic and bimetallic interfaces. Moreover, the work by Camacho and Ortiz [5] is also considered. They define, in fact, an effective opening displacement as a function of the opening (mode I) and sliding (mode II) interfacial displacements and introduce a coupling rule in order to account for both.

In a recent work [6] the mechanical behaviour of tubular composite profiles bonded to apposite nodal devices has been investigated in a combined manner which accounts for both the kinematics of the tube and the cohesive behaviour of the bonding interface. The effects of shear strains within the thickness of the tube are also considered. Although internal stresses essentially accord to the axial regime, it is observed that shear strains and stresses originated by the interfacial interactions are present within the composite tube over the adhesive bonding zones. As a

* Corresponding author.
E-mail addresses: aorefice@unisa.it (A. Orefice), g.mancusi@unisa.it (G. Mancusi), l.feo@unisa.it (L. Feo), f.fraternali@unisa.it (F. Fraternali).

http://dx.doi.org/10.1016/j.compstruct.2016.10.117
0263-8223/© 2016 Elsevier Ltd. All rights reserved.

Notation

O	origin of the reference system
i_1, i_2, k	unit vectors (orthonormal)
r	radial coordinate
z	longitudinal coordinate (axial)
z_1	axial coordinate at the beginning of the cohesive zone
O_i	intersection between z-axis and the generic cross-section (i.e. O_1)
t_b	thickness of the bonding layer
L_b	length of cohesive zone
t	thickness of the composite tube
L	length of the composite tube
r_2	inner radius of the composite tube
r_3	outer radius of the composite tube
ζ	dimensionless axial coordinate over the cohesive zone : $\zeta = (z - z_1)/L_b$
ρ	dimensionless radial coordinate: $\rho = (r - r_2)/t$
$w(r,z)$	displacement field (axial)
$w_i(z)$	displacement field (axial) at a defined radial coordinate r_i
$f_i(r)$	polynomials of the radial coordinate
d_r	interfacial normal displacement
d_k	interfacial tangential displacement
λ_I, λ_{II}	coupling coefficients between the normal and tangential interfacial displacements
h	interfacial equivalent displacement
h_c	characteristic value of the interfacial displacement (related to a static fracture)
Φ_U	fracture energy (per unit surface)
$F(h)$	cohesive potential
t_{rk}	interfacial tangential traction (per unit surface)
t_{rr}	interfacial normal traction (per unit surface)
p	interfacial traction
p_c	strength of the cohesive interface
κ	secant slope of the cohesive interface law
$p_z(r)$	normal traction forces (per unit surface) applied at the loaded end of the system
T	resultant traction
T_{max}	failure load
γ_i	average shear strain over the inner half thickness of the composite tube
γ_o	average shear strain over the outer half thickness of the composite tube

consequence, the local behaviour of the composite profile is affected by them and the failure criterion should account for this.

In the present work a parametric numerical analysis has been carried out in order to investigate the strains and stresses within the tube accounting for the interfacial interactions distribution. Moreover, the load provoking the bonding failure is evaluated. The numerical model has been developed according to the mechanical model described in [6,7]. A preliminary assumption has been made: the nodal device stiffness has been considered extremely high in comparison with the tube stiffness, that is a condition which substantially occurs in practice. The considered parameters of the study include the thickness of the composite tube, the bonding lengths, the load entity over a monotonic loading path up to the failure (Fig. 1).

2. The mechanical model

The mechanical model considered in the present study is based on appropriate kinematic hypotheses [6,7] that allow to investigate how the shear strains can influence the system response in terms of displacements and failure load. The model, which is very general, is now proposed for studying the response of a pultruded tubular profile made of FRP when generic forces, for instance cohesive forces or active forces, act on the lateral surface of the tube. The main feature of this model is the simulation of the axial displacement field as a linear combination of generalised unknowns,$w_i(z)$, which assume the physical meaning of axial displacements at defined radial coordinates, r_i. Moreover, the combination coefficients are polynomials of the radial coordinate, $f_i(r)$, truncated at the second order terms:

$$w(r,z) = w_i(z) f_i(r) \quad (i = 1,2,3) \tag{1}$$

The geometry of the problem under consideration is shown in Figs. 2a and 2b, where symbols L,t,r_2 and r_3 denote the length, the thickness, the inner and the outer radius of the tube, while L_b is for the length over which the cohesive forces act.

Furthermore, $\mathbf{i}_1$, $\mathbf{i}_2$ and $\mathbf{k}$ represent the unit vectors of the orthonormal basis, with $\mathbf{k}$ aligned to the z-axis, while $\mathbf{i}_1$, $\mathbf{i}_2$ lying within the cross-section plane, as well as the point O is a global origin. The symbol O_1 denotes the intersection between the z-axis and the 1–1 cross section.

By virtue of axisymmetric geometry, it is possible to model the distribution of the cohesive forces (per unit of surface) acting over the bonding zone (i.e. the interfacial normal traction, t_{rr}, and the tangential interaction, t_{rk}) as a function of the conjugated displacements d_r and d_k (Fig. 3).

According to [6–7], the following potential is introduced:

$$F(h) = \Phi_U \left[1 - \left(1 + \frac{h}{h_c}\right) e^{-(h/h_c)}\right] \tag{2}$$

where h indicates the norm of the vector $\mathbf{h}$:

$$\mathbf{h} = \lambda_I d_r \mathbf{n} + \lambda_{II} d_k \mathbf{k} \tag{3}$$

with λ_I and λ_{II} the coupling coefficients between the normal and tangential interfacial displacements.

The corresponding interaction, $\mathbf{p}$, is assumed as follows:

$$\mathbf{p} = \frac{1}{\lambda_I} t_{rr}\ \mathbf{n} + \frac{1}{\lambda_{II}} t_{rk}\ \mathbf{k} = p \frac{\mathbf{h}}{h} \tag{4}$$

with the norm p being expressed by:

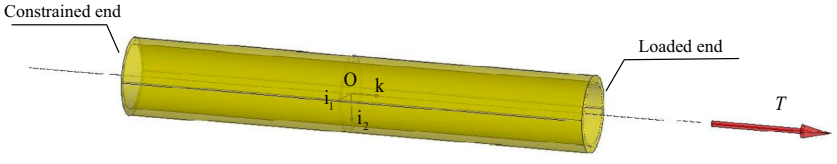

Fig. 1. Composite tube (axonometric view).

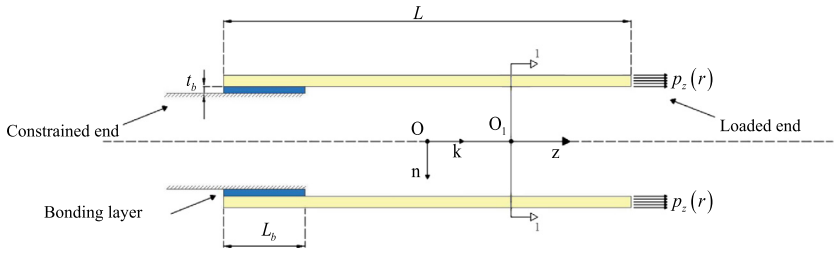

Fig. 2a. Geometric configuration (diametric longitudinal section).

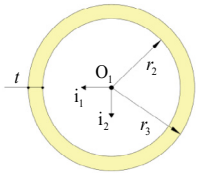

Fig. 2b. Geometric configuration (cross-section).

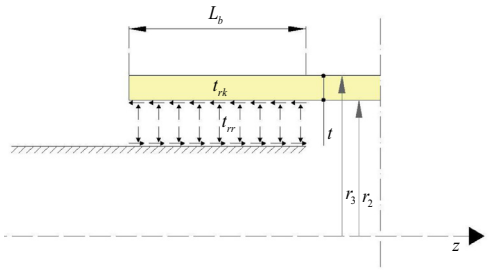

Fig. 3. Interfacial cohesive forces t_{rr} and t_{rk} (per unit surface).

$$p = \frac{dF}{dh} = p_c \frac{h}{h_c} e^{(1-h/h_c)} \tag{5}$$

Eq. (5) shows the dependency on the parameters h_c and p_c, related to the fracture energy (per unit surface):

$$\Phi_U = e p_c h_c \tag{6}$$

The expressions of h and p are finally obtained:

$$h = \sqrt{(\lambda_I d_r)^2 + (\lambda_{II} d_k)^2} \qquad p = \sqrt{\left(\frac{t_{rr}}{\lambda_I}\right)^2 + \left(\frac{t_{rk}}{\lambda_{II}}\right)^2} \tag{7.a-b}$$

It is also easy to observe that the cohesive model simulates the softening effect for $h > h_c$ while the full separation is achieved in an asymptotic sense (for $h \to \infty$).

3. Finite element model

A finite element approximation of the continuum problem above summarised is proposed in [6]. According to the numerical setup indicated in [6], the considered mesh is composed of two nodes finite elements (Fig. 4), with the single node having 6 degrees of freedom. The numerical approximation concerns the generalised kinematical unknowns $w_i(z)$

The interpolation of w_i is obtained by means of cubic Hermitian polynomials:

$$w_i(\xi) = h_{10}(\xi) w_i^{(1)} + h_{11}(\xi) w_i'^{(1)} + h_{20}(\xi) w_i^{(2)} + h_{21}(\xi) w_i'^{(2)} \tag{8}$$

where:

$$h_{10} = \frac{1}{4}(2 - 3\xi + \xi^3) \quad h_{11} = \frac{l_e}{8}(1 - \xi - \xi^2 + \xi^3) \tag{9.a-b}$$

$$h_{20} = \frac{1}{4}(2 + 3\xi - \xi^3) \quad h_{21} = \frac{l_e}{8}(-1 - \xi + \xi^2 + \xi^3) \tag{9.c-d}$$

being l_e the length of the finite element; $w_i^{(1)}$ and $w_i^{(2)}$ the nodal values of the kinematic unknown under consideration while $w_i'^{(1)}$ and $w_i'^{(2)}$ the nodal values of the derivative of w_i with respect to the axial coordinate z.

The following generalised displacements vector $\mathbf{w}_{(e)}$, with dimensions 3×1, is considered:

$$\mathbf{w}_{(e)} = [w_1, w_2, w_3]^T = \mathbf{N}\mathbf{U}_{(e)} \tag{10}$$

In previous expression $\mathbf{N}$ denotes the four-block matrix, with dimensions 3×12:

$$\mathbf{N} = [\mathbf{N}_{10}, \mathbf{N}_{11}, \mathbf{N}_{20}, \mathbf{N}_{21}] \tag{11}$$

where (p = 1, 2 and q = 0, 1):

$$\mathbf{N}_{pq} = \mathrm{diag}(h_{pq}, h_{pq}, h_{pq}) \tag{12}$$

Moreover, $\mathbf{U}_{(e)}$ is a numeric vector, with dimensions 12×1, which collects the values of the kinematic unknowns attained at both the nodes of the finite element:

$$\mathbf{U}_{(e)} = \left[\mathbf{U}_{(e,1)}^T, \mathbf{U}_{(e,2)}^T\right]^T \tag{13}$$

with $\mathbf{U}_{(e,p)}$ denoting the kinematic unknowns at the p node (p = 1, 2):

$$\mathbf{U}_{(e,p)} = \left[\left(w_1^{(p)}, w_2^{(p)}, w_3^{(p)}\right), \left(w_1'^{(p)}, w_2'^{(p)}, w_3'^{(p)}\right)\right]^T \tag{14}$$

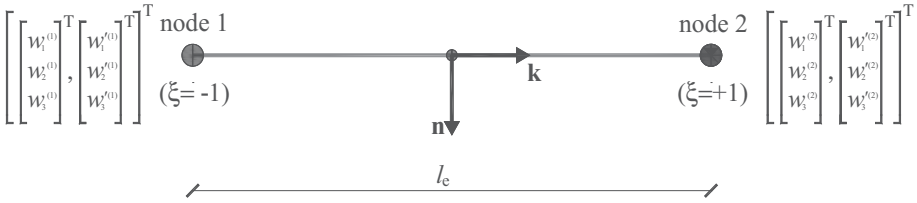

Fig. 4. Finite element.

With reference to the generic finite element, the interfacial displacements along both the n-axis (radial) and the z-axis, d_r and d_k, can be expressed as a function of the nodal unknowns $\mathbf{U}_{(e)}$.

If only mode II activates ($d_r = 0$), then $\mathbf{h} = \lambda_{II} d_k \mathbf{k}$. Under this assumption, the interfacial behaviour is represented by a unique cohesive relationship between t_{rk} and d_k. It results:

$$d_k = \mathbf{DNU}_{(e)} \tag{15}$$

with $\mathbf{D}$ the following numeric vector, with dimensions 1×3:

$$\mathbf{D} = [0, 1, 0] \tag{16}$$

Finally, the interfacial interaction along the z-axis, t_{rk}, is:

$$t_{rk} = \kappa d_k \tag{17}$$

where the symbol κ denotes the secant slope of the cohesive law:

$$\kappa = \lambda_{II} \frac{p_c}{h_c} e^{(1-\lambda_{II} d_k/h_c)} \tag{18}$$

If a non-linear solution exists (i.e. before collapse), it can be achieved by a numerical iterative algorithm which performs the updating of κ at any point of the numerical model for the new iteration.

4. Numerical results

The numerical analyses proposed in this paper deal with the response of a glass fibre-reinforced polymer (GFRP) tube bonded to a rigid substrate by means of a cohesive interface. An axisymmetric normal stress distribution $p_z(r)$ is considered (loaded end) as indicated in Fig. 5:

The resultant traction force, T, is:

$$T = 2\pi \int_{r_2}^{r_3} p_z(r) r dr \tag{19}$$

The main scope of the present paper is to investigate the effect of the cohesive forces on the strains and stresses within the tube. With the aim of pointing out this effect, three values of the wall thickness are considered (Table 1). Moreover, four values of the length of the cohesive zone have been associated with the generic thickness value.

The global length of the tube is fixed ($L = 10L_b$), thus guaranteeing that local effects at the loaded end do not interfere with local effects at the bonded end. The inner radius of the GFRP tube is fixed (66.0 mm); the thickness of the cohesive interface has been considered equal to t_b = 2.0 mm, which is a reasonable value when dealing with onsite bonding solutions.

Table 1
Geometry of the cohesive zone.

	Length of the cohesive zone – L_b	
Case 1 (t = 10 mm)	10t	100 mm
	20t	200 mm
	30t	300 mm
	40t	400 mm
Case 2 (t = 20 mm)	10t	200 mm
	20t	400 mm
	30t	600 mm
	40t	800 mm
Case 3 (t = 30 mm)	10t	300 mm
	20t	600 mm
	30t	900 mm
	40t	1200 mm

Table 2
GFRP constitutive properties.

Transverse normal modulus	(E_T = 3700 N/mm^2)
Longitudinal normal modulus	(E_L = 37,000 N/mm^2)
Shear modulus ($\mathbf{n} - \mathbf{k}$ plane)	(G_{TL} = 1850 N/mm^2)
Poisson coefficients	($\nu_{TT} = \nu_{TL} = \nu_{LT} = 0$)

Table 3
Parameters of the cohesive potential.

Fracture energy (per unit surface)	(Φ_U = 0.2 N mm/mm^2)
Characteristic value of h	(h_c = 0.0123 mm)
Mode I/mode II coupling coefficients	($\lambda_I = 0,\ \lambda_{II} = 1$)

The constitutive properties of the GFRP are presented in Table 2, while the parameters of the cohesive potential are indicated in Table 3.

It is important to remark that in the present study, which is a preliminary study, no coupling between mode I/mode II is considered, due to the assumption of zero Poisson coefficients for the GFRP.

Twelve numerical analyses have been performed as a combination of three thickness values with four lengths of the cohesive zone. The strain-stress behaviour has been studied over the loading

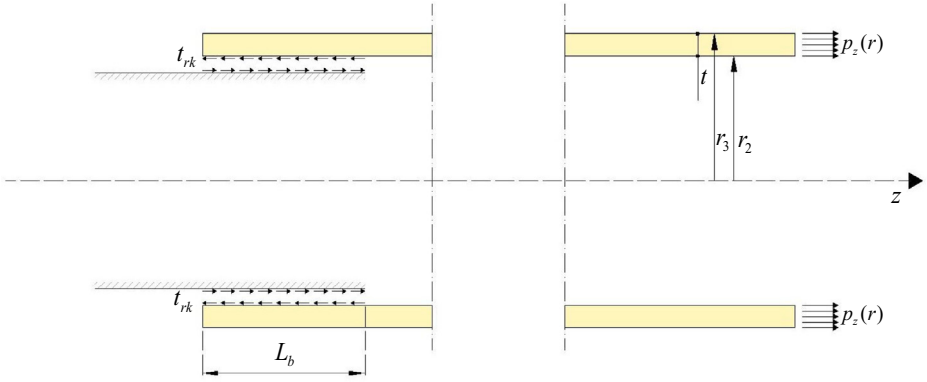

Fig. 5. Cohesive forces and external applied forces at the ends of the tube.

Table 4
Failure loads (numeric).

		$L_b = 10t$	$L_b = 20t$	$L_b = 30t$	$L_b = 40t$
Case 1 ($t = 10$ mm)	T_{max}[N]	158,250	170,000	171,000	171,000
	$F(h_{max})/\Phi_U$	0.990	0.995	0.999	0.999
Case 2 ($t = 20$ mm)	T_{max}[N]	247,300	257,000	257,000	257,000
	$F(h_{max})/\Phi_U$	0.985	0.990	0.992	0.992
Case 3 ($t = 30$ mm)	T_{max}[N]	325,800	337,000	338,000	338,000
	$F(h_{max})/\Phi_U$	0.985	0.995	0.999	0.999

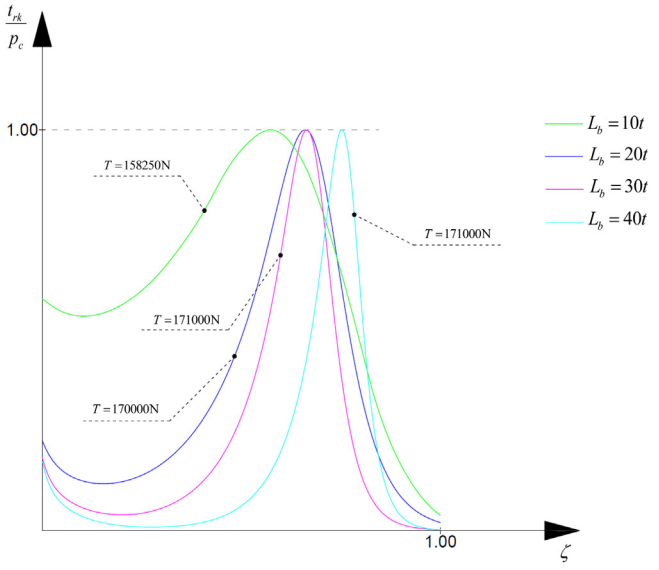

Fig. 6. Interfacial cohesive forces over the bonding zone at collapse (Case 1).

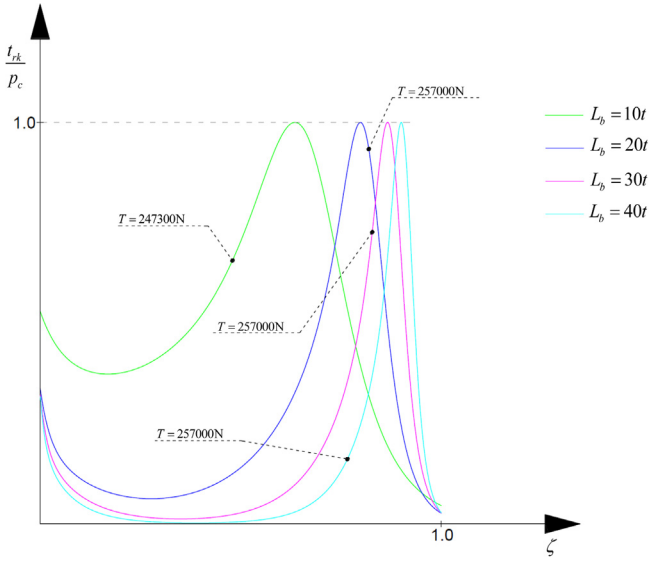

Fig. 7. Interfacial cohesive forces at collapse over the bonding zone (Case 2).

path up to the failure, which occurs as the separation of the tube from the substrate.

The prediction of the failure load, T_{max}, is presented in Table 4. In addition, the corresponding ratio of the stored interfacial energy to the fracture energy, $F(h_{max})/\Phi_U$, is also indicated.

As it is well-known, the failure load does not increase as the length L_b increases above a certain threshold value, more or less equal to $L_b = 20t$ for the considered problem.

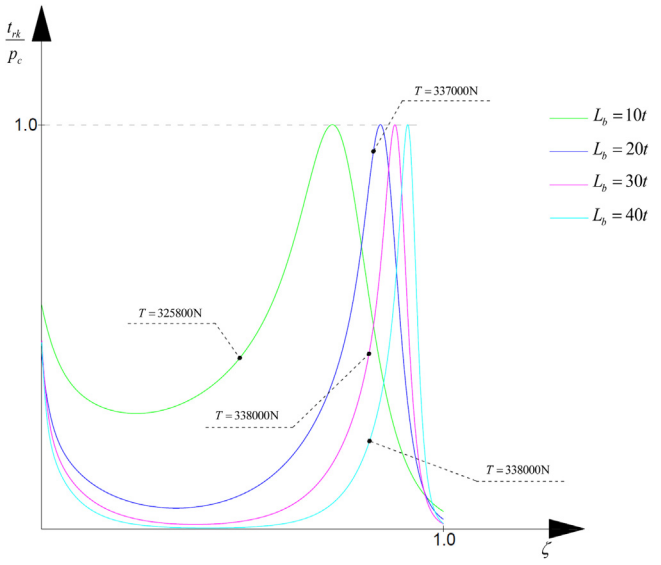

Fig. 8. Interfacial cohesive forces at collapse over the bonding zone (Case 3).

In Figs. 6–8, the interfacial cohesive forces t_{rk} at collapse are plotted in a dimensionless manner. They are normalized, in fact, with reference to the peak value corresponding to the strength of the interface. Also the axial coordinate has been normalised with respect to the global length of the bonding zone.

Several considerations are appropriate.

i) The full separation of the interface is achieved at $\zeta = 1.0$. This condition can be detected in a numeric sense if the ratio of the stored interfacial energy to the fracture energy becomes higher than an arbitrary fixed value (0.980 in the present study).
ii) The peak value of the interactions shifts towards the right end (the inner end) of the cohesive zone as L_b increases.
iii) The secondary peak at the opposite end of the bonding zone (left end – $\zeta = 0.0$) depends on the ratio between the stiffness of the substrate to the tube stiffness. The higher the ratio the lower the secondary peak.

In Table 5 the axial displacements at collapse ($T = T_{max}$) are presented for different cross-sections over the bonding length ($\zeta = 0.0$, $\zeta = 0.5$ and $\zeta = 1.0$), being here the place where the effects of the shear deformability of the GFRP tube are mostly expected. The values indicated in Table 5 are relative to the inner lateral surface (r_2), the mid-surface (r_m) and the outer lateral surface (r_3) of the tube.

Moreover, in Figs. 9–12 the graphs of the axial displacements (at collapse) are plotted versus the dimensionless radial coordinate ρ. They refer to the inner cross-section ($\zeta = 1.0$), where the full separation occurs.

Table 5
Axial displacements of the GFRP tube for three cross-sections over the cohesive zone.

		$L_b = 10t$			$L_b = 20t$			$L_b = 30t$			$L_b = 40t$		
		w_2[mm]	w_m[mm]	w_3[mm]	w_2[mm]	w_m[mm]	w_3[mm]	w_2[mm]	w_m[mm]	w_3[mm]	w_2[mm]	w_m[mm]	w_3[mm]
Case 1 ($t = 10$ mm)	$\zeta = 0.0$	0.003	0.010	0.012	0.001	0.003	0.004	0.001	0.002	0.003	0.001	0.002	0.002
	$\zeta = 0.5$	0.012	0.022	0.024	0.009	0.015	0,017	0.011	0.015	0.016	0.013	0.014	0.014
	$\zeta = 1.0$	0.058	0.060	0.061	0.092	0.093	0.093	0.131	0.131	0.131	0.136	0.136	0.136
Case 2 ($t = 20$ mm)	$\zeta = 0.0$	0.003	0.013	0.016	0.002	0.006	0.007	0.002	0.006	0.007	0.002	0.006	0.007
	$\zeta = 0.5$	0.038	0.051	0.055	0.019	0.022	0.024	0.027	0.028	0.028	0.036	0.036	0.036
	$\zeta = 1.0$	0.081	0.084	0.085	0.106	0.108	0.109	0.124	0.126	0.127	0.142	0.144	0.145
Case 3 ($t = 30$ mm)	$\zeta = 0.0$	0.003	0.017	0.020	0.003	0.012	0.013	0.003	0.011	0.013	0.003	0.011	0.013
	$\zeta = 0.5$	0.018	0.034	0.039	0.034	0.038	0.039	0.051	0.052	0.052	0.067	0.067	0.067
	$\zeta = 1.0$	0.093	0.097	0.100	0.133	0.137	0.138	0.176	0.178	0.180	0.209	0.211	0.212

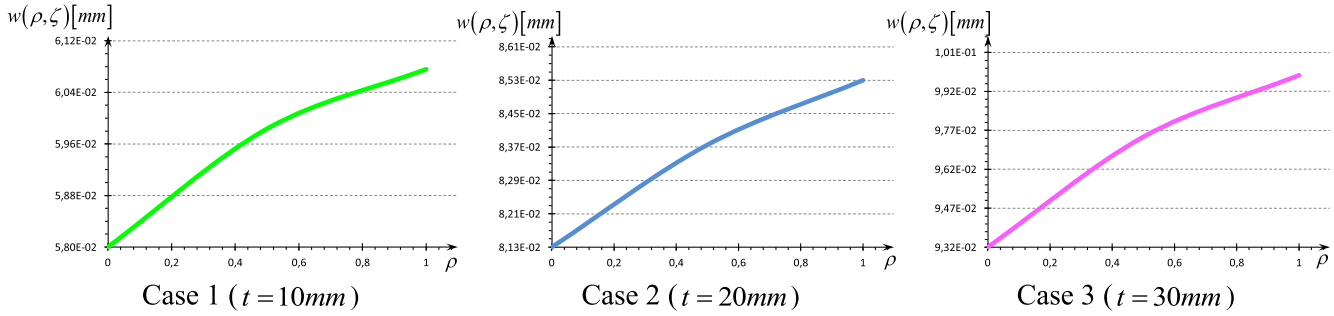

Fig. 9. Axial displacements versus the radial coordinate ($\zeta = 1.0$, $L_b = 10t$).

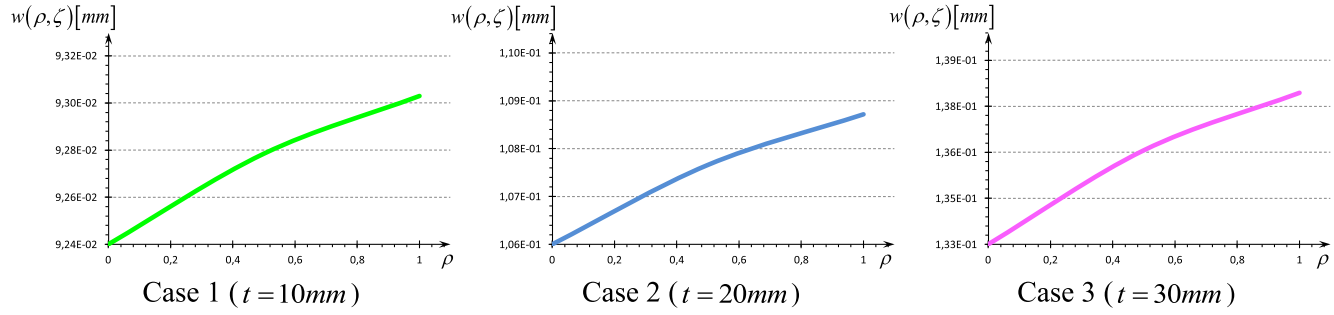

Fig. 10. Axial displacements versus the radial coordinate ($\zeta = 1.0$, $L_b = 20t$).

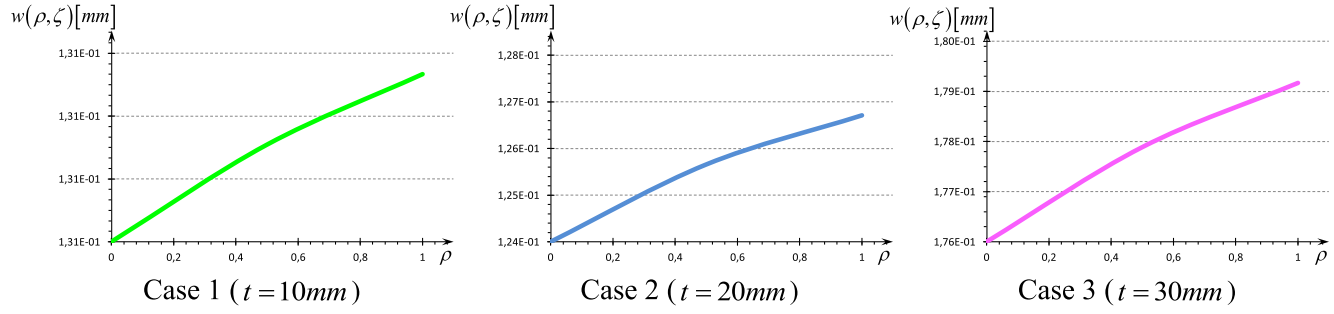

Fig. 11. Axial displacements versus the radial coordinate ($\zeta = 1.0$, $L_b = 30t$).

A simple consideration emerges: the gradient of the axial displacements within the thickness of the GFRP tube is responsible for evident non-uniform shear strains.

These strains can be appreciated in a simplified manner by means of the following formulas, which represent the average shear strains over the inner and outer half-thickness of the tube:

$$\gamma_i = \frac{w_m - w_2}{t/2} \qquad \gamma_o = \frac{w_3 - w_m}{t/2} \tag{20.a-b}$$

In Table 6 the shear strain analysis (at collapse) for the considered numerical simulations is presented.

The shear strains (averaged) have been analysed over the entire loading path up to the failure in order to detect the influence of the

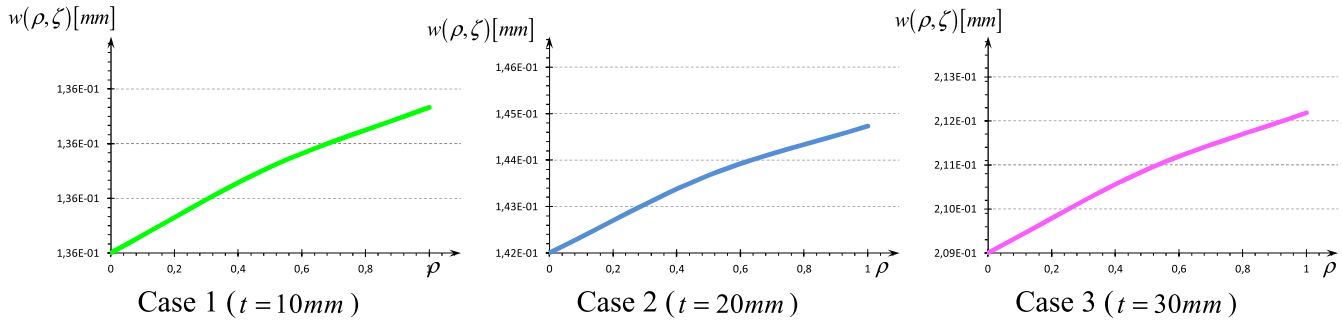

Fig. 12. Axial displacements versus the radial coordinate ($\zeta = 1.0,\ L_b = 40t$).

Table 6
Averaged shear strains (at collapse) within the thickness of GFRP tube.

		$L_b = 10t$		$L_b = 20t$		$L_b = 30t$		$L_b = 40t$	
		γ_i	γ_o	γ_i	γ_o	γ_i	γ_o	γ_i	γ_o
Case 1 ($t = 10$ mm)	$\zeta = 0.0$	1.34E−03	4.55E−04	3.94E−04	1.07E−04	2.83E−04	6.55E−05	2.66E−04	5.91E−05
	$\zeta = 0.5$	2.00E−03	5.56E−04	1.20E−03	3.99E−04	7.44E−04	2.66E−04	1.66E−04	6.24E−05
	$\zeta = 1.0$	3.67E−04	1.85E−04	7.70E−05	4.90E−05	9.27E−06	6.73E−06	9.00E−06	6.60E−06
Case 2 ($t = 20$ mm)	$\zeta = 0.0$	1.01E−03	3.07E−04	4.59E−04	9.76E−05	4.32E−04	8.75E−05	4.31E−04	8.71E−05
	$\zeta = 0.5$	1.31E−03	3.45E−04	3.72E−04	1.37E−04	7.44E−05	2.79E−05	1.51E−05	5.92E−06
	$\zeta = 1.0$	2.45E−04	1.55E−04	1.66E−04	1.06E−04	1.66E−04	1.05E−04	1.66E−04	1.05E−04
Case 3 ($t = 30$ mm)	$\zeta = 0.0$	8.99E−04	2.34E−04	5.90E−04	1.15E−04	5.78E−04	1.10E−04	5.77E−04	1.10E−04
	$\zeta = 0.5$	1.06E−03	3.37E−04	2.24E−04	8.20E−05	5.11E−05	1.89E−05	9.65E−06	3.68E−06
	$\zeta = 1.0$	2.83E−04	1.58E−04	2.04E−04	1.25E−04	1.26E−04	8.59E−05	1.26E−04	8.59E−05

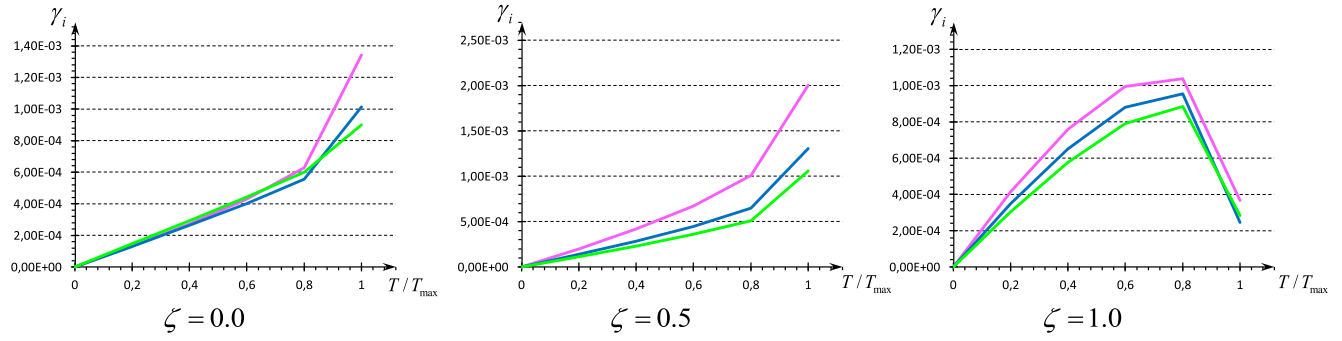

Fig. 13. Average shear strain γ_i versus applied load ($L_b = 10t$) (— $t = 10$ mm, — $t = 20$ mm, — $t = 30$ mm).

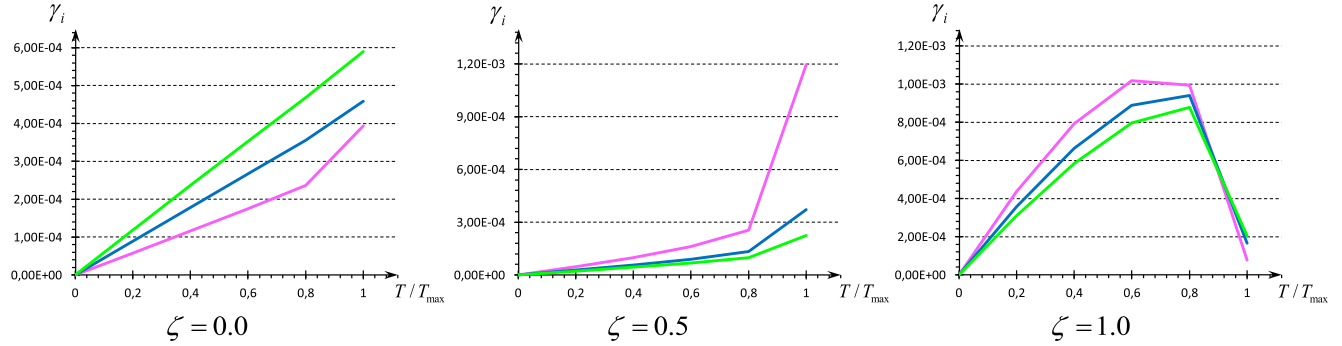

Fig. 14. Average shear strain γ_i versus applied load ($L_b = 20t$) (— $t = 10$ mm, — $t = 20$ mm, — $t = 30$ mm).

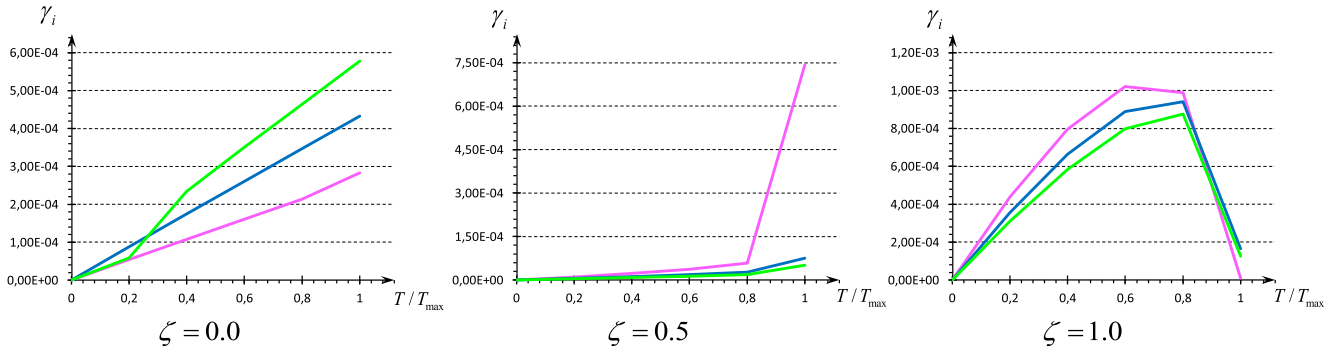

Fig. 15. Average shear strain γ_i versus applied load ($L_b = 30t$) (— $t = 10$ mm, — $t = 20$ mm, — $t = 30$ mm).

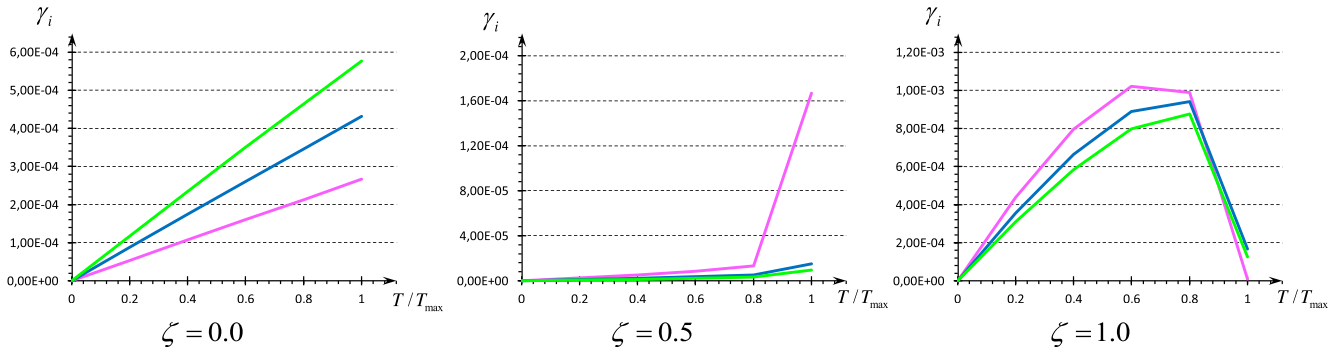

Fig. 16. Average shear strain γ_i versus applied load ($L_b = 40t$) (— $t = 10$ mm, — $t = 20$ mm, — $t = 30$ mm).

Table 7
Shear strains within the thickness of GFRP tube over the cohesive zone ($\zeta = 0.0$).

		$L_b = 10t$			$L_b = 20t$			$L_b = 30t$			$L_b = 40t$		
	T/T_{max}	T[N]	γ_i	γ_o	T[N]	γ_i	γ_o	T[N]	γ_i	γ_o	T[N]	γ_i	γ_o
Case 1 ($t = 10$ mm)	0.2	31,650	1.32E−04	4.13E−05	34,000	5.79E−05	1.34E−05	34,200	5.39E−05	1.18E−05	34,200	5.36E−05	1.18E−05
	0.4	63,300	2.72E−04	8.60E−05	68,000	1.16E−04	2.70E−05	68,400	1.07E−04	2.37E−05	68,400	1.07E−04	2.36E−05
	0.6	94,950	4.29E−04	1.37E−04	102,000	1.75E−04	4.10E−05	102,600	1.61E−04	3.56E−05	102,600	1.60E−04	3.53E−05
	0.8	126,600	6.28E−04	2.04E−04	136,000	2.37E−04	5.62E−05	136,800	2.14E−04	4.75E−05	136,800	2.13E−04	4.71E−05
	1.0	158,250	1.34E−03	4.55E−04	170,000	3.94E−04	1.07E−04	171,000	2.83E−04	6.55E−05	171,000	2.66E−04	5.91E−05
Case 2 ($t = 20$ mm)	0.2	49,460	1.30E−04	3.38E−05	51,400	8.93E−05	1.80E−05	51,400	8.75E−05	1.73E−05	51,400	8.74E−05	1.73E−05
	0.4	98,920	2.63E−04	6.89E−05	102,800	1.78E−04	3.62E−05	102,800	1.74E−04	3.48E−05	102,800	1.74E−04	3.47E−05
	0.6	148,380	4.01E−04	1.06E−04	154,200	2.67E−04	5.45E−05	154,200	2.61E−04	5.22E−05	154,200	2.61E−04	5.21E−05
	0.8	197,840	5.55E−04	1.50E−04	205,600	3.55E−04	7.31E−05	205,600	3.46E−04	6.97E−05	205,600	3.46E−04	6.95E−05
	1.0	247,300	1.01E−03	3.07E−04	257,000	4.59E−04	9.76E−05	257,000	4.32E−04	8.75E−05	257,000	4.31E−04	8.71E−05
Case 3 ($t = 30$ mm)	0.2	65,160	1.46E−04	3.31E−05	67,400	1.18E−04	2.22E−05	67,600	1.18E−04	2.20E−05	67,600	1.18E−04	2.18E−05
	0.4	130,320	2.93E−04	6.69E−05	134,800	2.36E−04	4.45E−05	135,200	2.34E−04	4.38E−05	135,200	2.34E−04	4.37E−05
	0.6	195,480	4.42E−04	1.02E−04	202,200	3.52E−04	6.69E−05	202,800	3.50E−04	6.58E−05	202,800	3.50E−04	6.58E−05
	0.8	260,640	5.99E−04	1.41E−04	269,600	4.68E−04	8.96E−05	270,400	4.64E−04	8.80E−05	270,400	4.64E−04	8.79E−05
	1.0	325,800	8.99E−04	2.34E−04	337,000	5.90E−04	1.15E−04	338,000	5.78E−04	1.10E−04	338,000	5.77E−04	1.10E−04

nonlinear cohesive behaviour on the shear strains and stresses. Of course, this effect is expected as a local effect nearby the constrained end of the tube, where the cohesive forces act.

A nonlinear effect in terms of shear strains is identified over the cohesive zone for higher load levels (Figs. 13–16). This is a clear consequence of the equilibrium between shear stresses arising on the lateral surface of the tube and interfacial forces (per unit surface) lying on the softening branch of the cohesive law (Tables 7–9).

As a final result, it is worth interesting to consider the evolution of the axial strains by means of the following formula, which returns the average value of the axial strain over the cohesive zone with reference to the mid-surface of the GFRP tube :

$$\varepsilon_{avg} = (w_m(\zeta = 1) - w_m(\zeta = 0))/L_b \tag{21}$$

A nonlinear dependency of the average axial strain on the applied load emerges over the bonding length (Table 10).

In the following section a review of the main relevant results is discussed.

5. Conclusive remarks

The use of a novel kinematical model of a composite tube loaded in traction is proposed in this study in order to capture nonlinear shear stresses originated by the equilibrium with possible cohesive forces acting on the lateral surface of the member. The

Table 8
Shear strains within the thickness of GFRP tube over the cohesive zone ($\zeta = 0.5$).

		$L_b = 10t$			$L_b = 20t$			$L_b = 30t$			$L_b = 40t$		
	T/T_{max}	T[N]	γ_i	γ_o	T[N]	γ_i	γ_o	T[N]	γ_i	γ_o	T[N]	γ_i	γ_o
Case 1 ($t = 10$ mm)	0.2	31,650	1.99E−04	7.30E−05	34,000	4.65E−05	1.75E−05	34,200	1.06E−05	3.98E−06	34,200	2.41E−06	9.07E−07
	0.4	63,300	4.17E−04	1.51E−04	68,000	9.83E−05	3.69E−05	68,400	2.25E−05	8.49E−06	68,400	5.10E−06	1.90E−06
	0.6	94,950	6.69E−04	2.39E−04	102,000	1.61E−04	6.02E−05	102,600	3.68E−05	1.38E−05	102,600	8.32E−06	3.08E−06
	0.8	126,600	1.01E−03	3.49E−04	136,000	2.54E−04	9.47E−05	136,800	5.84E−05	2.20E−05	136,800	1.33E−05	5.06E−06
	1.0	158,250	2.00E−03	5.56E−04	170,000	1.20E−03	3.99E−04	171,000	7.44E−04	2.66E−04	171,000	1.66E−04	6.24E−05
Case 2 ($t = 20$ mm)	0.2	49,460	1.38E−04	5.06E−05	51,400	2.76E−05	1.03E−05	51,400	5.51E−06	2.09E−06	51,400	1.09E−06	4.11E−07
	0.4	98,920	2.84E−04	1.04E−04	102,800	5.69E−05	2.13E−05	102,800	1.13E−05	4.20E−06	102,800	2.25E−06	8.46E−07
	0.6	148,380	4.46E−04	1.62E−04	154,200	8.98E−05	3.36E−05	154,200	1.78E−05	6.65E−06	154,200	3.56E−06	1.34E−06
	0.8	197,840	6.49E−04	2.32E−04	205,600	1.32E−04	4.93E−05	205,600	2.63E−05	9.81E−06	205,600	5.24E−06	1.96E−06
	1.0	247,300	1.31E−03	3.45E−04	257,000	3.72E−04	1.37E−04	257,000	7.44E−05	2.79E−05	257,000	1.51E−05	5.92E−06
Case 3 ($t = 30$ mm)	0.2	65,160	1.13E−04	4.10E−05	67,400	2.14E−05	7.89E−06	67,600	4.04E−06	1.50E−06	67,600	7.70E−07	2.97E−07
	0.4	130,320	2.31E−04	8.35E−05	134,800	4.40E−05	1.62E−05	135,200	8.24E−06	3.03E−06	135,200	1.20E−06	9.33E−07
	0.6	195,480	3.59E−04	1.29E−04	202,200	6.79E−05	2.49E−05	202,800	1.27E−05	4.60E−06	202,800	2.14E−06	5.24E−07
	0.8	260,640	5.10E−04	1.82E−04	269,600	9.70E−05	3.56E−05	270,400	1.84E−05	6.90E−06	270,400	3.44E−06	1.23E−06
	1.0	325,800	1.06E−03	3.37E−04	337,000	2.24E−04	8.20E−05	338,000	5.11E−05	1.89E−05	338,000	9.65E−06	3.68E−06

Table 9
Shear strains within the thickness of GFRP tube over the cohesive zone ($\zeta = 1.0$).

		$L_b = 10t$			$L_b = 20t$			$L_b = 30t$			$L_b = 40t$		
	T/T_{max}	T[N]	γ_i	γ_o	T[N]	γ_i	γ_o	T[N]	γ_i	γ_o	T[N]	γ_i	γ_o
Case 1 ($t = 10$ mm)	0.2	31,650	4.14E−04	8.67E−05	34,000	4.37E−04	9.13E−05	34,200	4.39E−04	9.20E−05	34,200	4.39E−04	9.20E−05
	0.4	63,300	7.58E−04	1.74E−04	68,000	7.93E−04	1.83E−04	68,400	7.96E−04	1.84E−04	68,400	7.96E−04	1.85E−04
	0.6	94,950	9.96E−04	2.58E−04	102,000	1.02E−03	2.69E−04	102,600	1.02E−03	2.71E−04	102,600	1.02E−03	2.71E−04
	0.8	126,600	1.04E−03	3.22E−04	136,000	9.94E−04	3.25E−04	136,800	9.88E−04	3.26E−04	136,800	9.88E−04	3.26E−04
	1.0	158,250	3.67E−04	1.85E−04	170,000	7.70E−05	4.90E−05	171,000	9.27E−06	6.73E−06	171,000	9.00E−06	6.60E−06
Case 2 ($t = 20$ mm)	0.2	49,460	3.49E−04	6.24E−05	51,400	3.56E−04	6.32E−05	51,400	3.56E−04	6.31E−05	51,400	3.56E−04	6.31E−05
	0.4	98,920	6.52E−04	1.28E−04	102,800	6.64E−04	1.30E−04	102,800	6.63E−04	1.30E−04	102,800	6.63E−04	1.30E−04
	0.6	148,380	8.79E−04	1.97E−04	154,200	8.89E−04	2.00E−04	154,200	8.88E−04	1.99E−04	154,200	8.89E−04	1.99E−04
	0.8	197,840	9.54E−04	2.63E−04	205,600	9.41E−04	2.65E−04	205,600	9.41E−04	2.65E−04	205,600	9.41E−04	2.64E−04
	1.0	247,300	2.45E−04	1.55E−04	257,000	1.66E−04	1.06E−04	257,000	1.66E−04	1.05E−04	257,000	1.66E−04	1.05E−04
Case 3 ($t = 30$ mm)	0.2	65,160	3.05E−04	4.92E−05	67,400	3.09E−04	4.91E−05	67,600	3.10E−04	4.92E−05	67,600	3.10E−04	4.92E−05
	0.4	130,320	5.76E−04	1.02E−04	134,800	5.83E−04	1.02E−04	135,200	5.84E−04	1.02E−04	135,200	5.84E−04	1.02E−04
	0.6	195,480	7.91E−04	1.59E−04	202,200	7.96E−04	1.59E−04	202,800	7.97E−04	1.59E−04	202,800	7.97E−04	1.59E−04
	0.8	260,640	8.86E−04	2.19E−04	269,600	8.78E−04	2.20E−04	270,400	8.77E−04	2.20E−04	270,400	8.77E−04	2.20E−04
	1.0	325,800	2.83E−04	1.58E−04	337,000	2.04E−04	1.25E−04	338,000	1.26E−04	8.54E−05	338,000	1.26E−04	8.59E−05

Table 10
Axial strain analysis over the bonding length.

		$L_b = 10t$		$L_b = 20t$		$L_b = 30t$		$L_b = 40t$	
	T/T_{max}	T [N]	ε_{avg} [$\mu\varepsilon$]	T [N]	ε_{avg} [$\mu\varepsilon$]	T [N]	ε_{avg} [$\mu\varepsilon$]	T [N]	ε_{avg} [$\mu\varepsilon$]
Case 1 ($t = 10$ mm)	0.2	31,650	58	34,000	40	34,200	31	34,200	26
	0.4	63,300	119	68,000	82	68,400	64	68,400	54
	0.6	94,950	188	102,000	130	102,600	100	102,600	84
	0.8	126,600	273	136,000	191	136,800	146	136,800	122
	1.0	158,250	497	170,000	449	171,000	430	171,000	335
Case 2 ($t = 20$ mm)	0.2	49,460	42	51,400	32	51,400	27	51,400	25
	0.4	98,920	86	102,800	65	102,800	55	102,800	50
	0.6	148,380	133	154,200	100	154,200	84	154,200	77
	0.8	197,840	189	205,600	140	205,600	117	205,600	105
	1.0	247,300	353	257,000	254	257,000	200	257,000	172
Case 3 ($t = 30$ mm)	0.2	65,160	37	67,400	31	67,600	29	67,600	26
	0.4	130,320	75	134,800	62	135,200	56	135,200	53
	0.6	195,480	115	202,200	94	202,800	85	202,800	80
	0.8	260,640	159	269,600	129	270,400	115	270,400	108
	1.0	325,800	268	337,000	208	338,000	186	338,000	166

model is limited to axisymmetric geometric conditions (annular cross-section) and is able in general to account for the coupling between mode I/mode II. A preliminary parametric analysis indicates the need for considering local nonlinear shear strains in evaluating the response of the composite tube, as well as the influence of such strains on the average axial strain of the system over the length where the cohesive forces act. The obvious evolution of the present study will concern the response of the tube under applied dynamic traction force (cyclic).

Acknowledgments

This research was supported by the Italian Research Program ReLUIS-DPC 2014-2018.

References

[1] Almitani KH, Othman R. Analytical solution of the harmonic response of visco-elastic adhesively bonded single-lap and double-lap joints. Int J Adhes Adhes 2016;71:55–65.

[2] Xu Q, Qu S. Irreversible deformation of metal matrix composites: a study via the mechanism-based cohesive zone model. Mech Mater 2015;89:72–84.

[3] Rose JH, Ferrante J, Smith JR. Universal binding energy curves for metals and bimetallic interfaces. Phys Rev Lett 1981;47:675–8.

[4] Rose JH, Smith JR, Ferrante J. Universal features of bonding in metals. Phys Rev B 1983;28:1835–45.

[5] Camacho GT, Ortiz M. Computational modelling of impact damage in brittle materials. Int J Solids Struct 1996;33:2899–938.

[6] G. Mancusi, A. Orefice, L. Feo, F. Fraternali, Structural analysis of adhesive bonding for thick-walled tubular composite profiles, ECCOMAS Congress, 2016.

[7] G. Mancusi, Elastic Behaviour of Thick-Walled Composite Tubes, Submitted to Composite Structures.